Preprint version, Reference: Patnayakuni RP, Pulatso B, Lourenço PB, Azenha M, Pereira JM (2020), A meso-scale discrete element method framework to simulate thermo-mechanical failure of concrete subjected to elevated temperatures. Engineering Fracture Mechanics, 239, 107269. https://doi.org/10.1016/j.engfracmech.2020.107269

A meso-scale discrete element method framework to simulate thermo-mechanical failure of concrete subjected to elevated temperatures

P. Ravi Prakash[a], Bora Pulatsu[b], P. B. Lourenço[c], Miguel Azenha[c], João M. Pereira[c]

Abstract: This paper presents mesoscale thermo-mechanical analyses of plain (unreinforced) concrete based on the discrete element method (DEM). The proposed discontinuum modelling strategy represents the aggregates and matrix as a system of deformable polyhedral blocks, interacting along their boundaries. The nodal velocities of each block are calculated via the explicit integration scheme of DEM, and contact stresses are computed based on the relative contact displacements of the adjacent blocks. To better predict the thermo-mechanical behaviour of concrete, fracture energy-based contact constitutive models are implemented by considering temperature dependency at the zone and contact properties. First, the discrete meso models are tested under uniaxial compression loading at room temperature. Then, transient thermo-mechanical tests are performed considering different load levels. The results of the computational models are compared with the macroscopic response quantities of concrete obtained from the available experimental studies in the literature. The results indicate that the developed DEM framework predicts the complex mesoscale thermo-mechanical response history and the typical damage progression observed in concrete. Furthermore, the fracture patterns, crack propagation with temperature, and the differential thermal expansion phenomena are studied in detail.

Keywords: Discrete element method, Concrete, Fire, Contact Mechanics, Thermo-mechanical analysis

[a] Civil Engineering Discipline, National Institute of Technology Warangal, Email: rprakash@nitw.ac.in (Corresponding Author)
[b] University of Nebraska-Lincoln
[c] Institute for Sustainability and Innovation in Structural Engineering, University of Minho

1 Introduction

Concrete is one of the most commonly used construction materials. In addition to usual service loads, concrete structures carry the risk of being exposed to fire. Concrete, when subjected to elevated temperatures, is characterized by thermal expansion, thermal shrinkage, and degradation in strength and stiffness. Such phenomena eventually culminate in a thermo-mechanical strain, which is dependent on thermal and mechanical loading histories, respectively. The understanding and characterization of thermo-mechanical strain have gained significant attention of researchers in the past decades. The early studies in this context included the works of Hasen and Eriksson [1] and Anderberg and Thelandersson [2]. In such early studies, reduction in thermal strain was observed in the transient thermo-mechanical experimental tests of concrete under constant compressive loading and is attributed to the load-induced thermal strain (LITS). It should be noted that the components of thermo-mechanical strain include elastic strain, free thermal strain (FTS), and LITS. LITS is irreversible, only observed in the first heating cycle, and is treated as quasi-instantaneous [2–4].

In the past decades, several terms have been used to describe the LITS and its components, which include transient strain, transient creep, and transient thermal creep [5]. The physical meaning of these terms is interpreted differently by various researchers and has been a matter of discussion among researchers over the past 40 years [5,6]. State of the art review on the LITS in concrete by Torelli et al. [5] indicated the existence of several interdependent physical and chemical phenomena that contribute to the LITS. For instance, the drying creep phenomenon can lead to micro tensile strains, and these strains in conjunction with applied compressive stress will contribute to LITS during the initial phase of heating [7]. The other notable phenomena include calcium silicate hydrate (C-S-H) disintegration coupled with moisture transport [1] and micro-cracking due to the differential thermal expansion between the aggregates and cement matrix [3]. The C-S-H gel disintegration is predominant during the

initial stages of heating (up to 300-400 ˚C), whereas the differential thermal expansion is predominant in the later stages of heating [3,5]. Furthermore, a few experimental investigations [8] had demonstrated a higher level of LITS in the case of high-performance concrete (HPC) compared to ordinary concrete. This is due to higher effective stress in the concrete pores due to lower permeability in HPC, which curtails the rate of mass transport within concrete.

Several constitutive models have been developed by different researchers to simulate various components of the thermo-mechanical strain in the past decades [9]. These constitutive models have been implemented in various numerical models which work at various scales and predominantly rely on the finite element method (FEM). The early constitutive models for modelling the thermo-mechanical strain in concrete include the works of Anderberg and Thelandersson [2] and Schneider [10]. They are uniaxial based and have been successfully implemented in various 1-D macro numerical models (e.g. [11,12]). Later, Thelandersson [13] developed a 3-D constitutive framework for modelling the thermo-mechanical strain that was implemented in various 3-D FE frameworks (e.g. [14]). Majorana et al. [15] developed a 3-D FE framework with due consideration to LITS and fire-induced spalling phenomenon. Recently, Yao et al. [16] developed a thermodynamic based multi-axial constitutive model for modelling the various components of thermo-mechanical strain including LITS.

It is worth noting that the understanding of meso-scale thermo-mechanics in concrete subjected to fire exposure is still imprecise. Although the previously mentioned constitutive frameworks facilitate reasonably accurate thermo-mechanical predictions, those frameworks follow a phenomenological approach. Critical physical phenomena like the disintegration of C-S-H gel, differential thermal expansion of ingredients of concrete, etc. are not well explained in those phenomenological models, and has been a matter of discussion among researchers [9]. This limitation can be partly alleviated with the aid of detailed meso/micro model, which models aggregates, cement matrix, and interfacial transition zone (ITZ) separately. In general,

traditional FEM may not be a viable solution for modelling such discontinues due to discontinuity induced ill-posedness in the governing equations [17]. One of the feasible alternative numerical methods to address such limitation can be the discrete element method. The utilization of DEM for solving discontinuum mechanics problems has been receiving significant attention from researchers after it was first introduced by Cundall [18]. In the context of modelling discontinuities in concrete, DEM has been a strong alternative to discontinuous finite element methods in the recent past due to the increase in computational processing powers. In the purview of meso-scale modelling of concrete, different discontinuous modelling strategies associated to lattice, discrete and/or finite element methods are presented in the literature [19,20,21,22,23,24].

Regarding DEM modelling of thermo-mechanical strain in concrete, very limited studies are available in the literature. It is worth knowing that DEM facilitates a detailed understanding of the transient evolution of fracture patterns in concrete under thermo-mechanical loading, which is otherwise difficult in laboratory fire tests due to visibility constraints due to the furnace chamber enclosing the sample. Recently, Sinaie et al. [25] developed a particle-based DEM model and generated macroscopic temperature-dependent stress-strain curves in concrete. However, their studies are up to 400 ˚C only. Grassl and Pearce [26] developed a damage-based lattice element framework for understanding the meso-scale thermo-mechanics. However, their framework does not account for temperature-dependent material degradation. Moreover, the discussion on meso-scale thermo-mechanics in concrete and its contribution towards LITS is missing in the literature. This study presents a fracture mechanics based two-dimensional (2D) DEM model to be utilized in the meso-scale thermo-mechanical computations on concrete. Aggregates, cement mortar and ITZ are modelled explicitly in conjunction with the temperature-dependent interface nonlinearity. Through the present research, a commercial DEM Code 3DEC, developed by ITASCA [27], is used to perform

thermo-mechanical analysis. The adopted contact models are a new development, written in C++ and compiled as DLL (dynamic link library) into 3DEC via the user-defined constitutive model option.

The present paper is organized as indicated next. Section 2 presents the theoretical developmental aspects of the 2D DEM modelling approach, which include assumptions, thermo-mechanical components of the DEM model, and temperature-dependent contact models. Next, Section 3 and Section 4 presents the experimental validation study on concrete samples both at room temperature and at elevated temperatures. Finally, Section 5 concludes the present study with important inferences made regarding the proposed modelling strategy.

2 Theoretical framework

This section presents the formulation of the discrete meso-modelling approach that is applied to analyse thermo-mechanical behaviour of concrete subjected to uniaxial compression. Note that the discontinuum type of analysis using DEM can be performed in a precise manner using a 3D DEM framework [28]. However, such 3D DEM modelling is computationally intensive. Given the relatively randomized spatial distribution of aggregates in concrete, the aforementioned limitation can be alleviated with the aid of 2D plane stress DEM model, and such strategies have been successfully implemented in the past (e.g. [26]). Here, the morphology of ordinary concrete is represented using polyhedral blocks in a discontinuum based setting to replicate aggregate and cement matrix. In this research, polyhedral blocks are generated based on a Laguerre tessellation, using the open-source Neper software package (further applications and detailed information about the software can be found in [29–32]).

The illustration of a representative volume unit (RVU) of a concrete 2D DEM model is shown in Figure 1. Aggregates are assumed to be in an elastic continuum (using finite difference zones), whereas interface discontinuities are accounted for cement mortar and ITZ (using

nonlinear soft contact models or springs, with elastic stiffness given by K_n, normal, and K_s, tangential, with tension f_t, cohesion c, and friction angle ϕ), respectively. Different research investigations reported (e.g. [33,34]) that the aggregate-cement mortar interface region, also known as interfacial transition zone (ITZ) is similar to that of cement paste, however, with lesser strength due to relatively higher porosity compared to that of cement mortar. Henceforth, in the present study, to facilitate computationally efficient modelling, the properties of ITZ are lumped at the aggregate-mortar contact points, instead of modelling ITZ as separate polyhedral blocks. To generate discrete meso-models, a two-level discretization scheme is performed where the concrete morphology is discretized into polyhedral blocks, and these blocks are further discretized into finite difference tetrahedral zones, as depicted in Figure 1. The interacting grid points corresponding to neighbouring polyhedral blocks are designated as contact points (Figure 1). The thermal analysis works on zones, whereas the mechanical analysis works on zones and contact points of polyhedral blocks. It should be mentioned that the developed framework, in its present form, does not account for thermo-mechanical loading induced discontinuities in the heat transfer phenomena within the concrete.

The thermal-mechanical DEM analysis is performed using a staggered one-way coupling scheme. In such a scheme, the thermal analysis is performed on a fixed geometry first, followed by the mechanical DEM analysis at constant temperatures at various given time steps [35]. The theoretical aspects of the individual thermal and mechanical DEM analysis are discussed in Sections 2.1 and 2.2, respectively.

2.1 Thermal analysis

For a 2D body, as shown in Figure 1, the governing PDE to model the heat transfer is formulated from the law of energy balance and is given by

$$\left(\rho c\right)_T \frac{\partial T}{\partial t} = \nabla.\left(\gamma_T \nabla T\right), \tag{1}$$

where T represents temperature, $(\rho c)_T$ represents temperature-dependent specific heat capacity, $\boldsymbol{\gamma}_T$ is the temperature-dependent thermal conductivity tensor. The boundary conditions are applied in terms of temperature or the heat flux component vector normal to the boundary, and they include a) given temperature, b) heat flux component vector normal to the boundary, c) convective boundaries, and d) adiabatic boundaries. For instance, the governing PDE for the convective heat flux is written as

$$\left(\boldsymbol{\gamma}\nabla T\right).\mathbf{n} = -h_c\left(T - T_f\right), \tag{2}$$

where T_f represents the fire temperature, h_c (25 W/m^{2}K) represents the convective heat transfer coefficient. Finite difference discretization is applied to Equations (1) and (2) in an explicit setting within the grid points of polyhedral zones. This results in a highly nonlinear system of equations and is solved iteratively until the L_2 norm of temperature reaches the prescribed value of tolerance.

2.2 Mechanical DEM analysis

As mentioned previously, transient mechanical DEM analysis is executed in a one-way coupling scheme, with the temperature profiles of the previously executed thermal analysis as an input. In a meso-scale representation, discontinuities in concrete can be modelled in a precise manner with the aid of deformable polyhedral blocks with material nonlinearity effects imposed at the contact points. Note that in thermo-mechanical analysis, modelling additional physical phenomena, including thermal dilation, temperature-dependent material degradation, damage, and LITS effects are challenging. To circumvent these challenges, material nonlinearity with temperature-dependency is lumped at the contact points whereas the polyhedral blocks are assumed to be elastic. The deformability in the polyhedral blocks is attributed to the mechanical loading and thermal dilation effects. The proposed modelling

approach in its present form does not account the effects of C-S-H disintegration and isothermal creep. With this settle assumptions and idealizations, the equations of motion, solved for each grid point *i*, is written as

$$m\boldsymbol{u}_i + \xi m\boldsymbol{u}_i = \sum \boldsymbol{F}_i \tag{3}$$

where m represents the nodal mass, $\boldsymbol{u}_i$ represents the nodal displacement vector and ξ is the mass proportional viscous damping. $\sum \mathbf{F}_i$ indicates the nodal resultant force vector and is computed as

$$\sum \mathbf{F}_i = \mathbf{F}_g + \mathbf{F}_z + \mathbf{F}_c + \mathbf{F}_e \tag{4}$$

where $\mathbf{F}_g$, $\mathbf{F}_z$, $\mathbf{F}_c$, and $\mathbf{F}_e$ denote gravity, internal, contact, and external forces, respectively, at the grid point. The internal forces $\mathbf{F}_z$ in the grid points are due to the stresses generated in the zones adjacent to grid points and is written as

$$\begin{aligned} \mathbf{F}_z &= \int \boldsymbol{\sigma} \cdot \mathbf{n} ds = \int \mathbf{D}_T(\boldsymbol{\varepsilon}_m) \mathbf{n} ds, \\ \boldsymbol{\varepsilon}_m &= \boldsymbol{\varepsilon}_t - \boldsymbol{\varepsilon}_{Th}, \\ \boldsymbol{\varepsilon}_{Th} &= \alpha \Delta T, \end{aligned} \tag{5}$$

where $\boldsymbol{\sigma}$ represents the zone stress tensor, $\mathbf{n}$ represents the outward normal, $\mathbf{D}_T$ represents the temperature-dependent elastic constitutive matrix, T represents temperature, and α is the thermal expansion coefficient. $\boldsymbol{\varepsilon}_t, \boldsymbol{\varepsilon}_m$ and $\boldsymbol{\varepsilon}_{Th}$ represent total strain, thermo-mechanical strain, and thermal strain, respectively. As detailed in [5], the LITS is characterized by damage due to differential thermal expansion between aggregates and cement mortar, C-S-H disintegration coupled with moisture transport and isothermal creep. The zone constitutive models in their present form do not account for damage due to C-S-H gel disintegration and isothermal creep. This is due to the lack of relevant detailed experimental characterization at the individual ingredient level. As will be shown in Section 4, and such idealizations result in deviations

from the experimental observations at elevated temperatures. However, it is important to note the proposed modelling strategy provides a detailed representation of constituents in concrete; therefore, differential thermal expansion between aggregates and cement mortar, which contributes to LITS, is accounted for during the analysis. Moreover, the C-S-H gel disintegration is significant during the initial stages of heating (up to 300-400 ˚C), whereas the differential thermal expansion is significant in the later stages of heating [3,5]. Therefore, given the mentioned limitations, such idealizations within the meso-scale framework are acceptable and have been successfully implemented by earlier studies as well (e.g. [26]).

Equation (3) is solved using a central difference method (see Equation (7)), with a time step Δt discretized into two equal intervals. The nodal velocities here are calculated in an explicit integration setting with local damping as given by Cundall [36] (see Equation (6)).

$$\ddot{\mathbf{u}}_i^t = \frac{\dot{\mathbf{u}}_i^{t+\Delta t/2} - \dot{\mathbf{u}}_i^{t-\Delta t/2}}{\Delta t} \tag{6}$$

$$\dot{\mathbf{u}}_i^{t+\Delta t/2} = \dot{\mathbf{u}}_i^{t-\Delta t/2} + \left[\sum \mathbf{F}_i^t - (\mathbf{F}_d)_i\right]\frac{\Delta t}{m}, \tag{7}$$

The local damping forces $(F_d)_i$ which oppose motion are proportional to the unbalanced forces and are calculated as

$$(\mathbf{F}_d)_i = \lambda \left|\sum \mathbf{F}_i^t\right| sgn\left(\dot{u}_i^{t-\Delta t/2}\right), \tag{8}$$

where λ is the dimensionless damping constant (default value is 0.8). In the case of local damping formulation, spatially varying damping is required in the numerical model to facilitate progressive collapse [37]. In an explicit finite difference solution algorithm, to facilitate the numerical stability, the limiting time step is obtained as

$$\Delta t = 2\sqrt{m/k_{gp}} \tag{9}$$

where k_{gp} is the nodal stiffness obtained by adding zone and contact (only the grid point on the faces) stiffness [38].

It should be mentioned that at every finite difference iteration, using Equations (6) and (7), the locations and relative displacements of blocks are updated. Utilizing these relative contact displacements among the adjacent blocks (Δu_n in the normal direction and Δu_s in the tangential direction), at a given temperature *T*, the new incremental normal stress $(\Delta\sigma)$ and incremental shear stress $(\Delta\tau)$ at the contact points are computed. In the elastic regime, these incremental stresses are calculated as

$$\begin{aligned} \Delta\sigma &= K_{n,T}\Delta u_n, \\ \Delta\tau &= K_{s,T}\Delta u_s, \end{aligned} \tag{10}$$

where, $K_{n,T}$ and $K_{s,T}$ denote the temperature-dependent contact stiffness in normal and tangential directions, respectively. Subsequently, obtained incremental stresses are added to the contact stresses recorded from the previous iteration, and they are corrected (if applicable) in accordance with the contact constitutive models; such procedure will be discussed subsequently. Finally, the contact forces are determined by multiplying the stresses with the related contact area, and such forces are substituted back in Equation (7). Thus, the dynamic solution scheme of the mechanical analysis continues until quasi-static equilibrium is reached. The proposed solution algorithm, developed within the DEM framework, to analyse the thermo-mechanical behaviour of concrete is shown in Figure 2. Note that the one-way thermo-mechanical coupling is performed by programming FISH functions (an executable programming language in 3DEC, [27]).

The mechanical response of the developed DEM framework is governed by temperature-dependent nonlinear contact models along with the thermo-elastic constitutive behaviour of the polyhedral blocks. Therefore, the potential failure modes of concrete are simulated at the

contact points, which are associated with tension, compression, and shear contact constitutive relations. Note that in this study, the tension and shear constitutive behaviour of the contact is governed by a temperature-dependent Mohr-Coulomb failure envelope.

Figure 3 schematically depicts the temperature-dependency in such envelope, with contraction of the envelope with the increase in temperature.

Such an interface failure envelope is characterized by the temperature-dependent tensile strength ($f_{t,T}$), temperature-dependent cohesion (c_T) and temperature-dependent friction angle (ϕ). The contact stresses remain in the elastic regime if the following criteria are met.

$$\begin{aligned} &\sigma_n\big|_{\text{Tension}} \le f_{t,T}, \\ &\tau \le c_T + \sigma_n \tan\phi. \end{aligned} \tag{11}$$

It is noted that the failure criteria in tension and shear modes are assumed to be decoupled in the present study, similar to [39]. Further, at a given temperature *T*, the failure envelopes in tension and shear undergo contraction during the further course of loading (envelope-1 to envelope-2, see (Figure 3), governed by the respective softening constitutive models discussed below. Furthermore, the damage parameters (δ_s and δ_t) shown in Figure 3, are quantified at each mechanical iteration and are carried forward to subsequent time steps. Such carry forward operations pertaining to the damage variables facilitate precise thermo-mechanical formulation. In the case of characterization of macro-scale uniaxial compressive response of concrete, in the purview of present study, significant strain hardening is observed [2,10]. Such a phenomenon is accounted for in the contact model in addition to the tension and shear failure modes by a bi-linear contact model in the compression regime. As will be shown in Section 3.1, such contact model in compression regime facilitates accurate model predictions and has been successfully implemented in the past (e.g. [25]) as well.

The contact tensile and shear stresses can be updated from the softening constitutive relations, deduced from fracture mechanics principles. Due to their physically precise formulation, such an approach has been gaining significant attention of researchers in the recent past. Recently, Pulatsu et al. [40] developed contact constitutive models in tension and shear regimes, respectively using mode-1 (G_{f1}) and mode-2 (G_{f2}) fracture energies for the DEM analysis of masonry structures. Detailed theoretical developmental and implementation aspects for such models can be found in [40], not repeated here for the sake of brevity. In this framework, these contact models are extended to include the effects of temperature-dependent material nonlinearity. At a given temperature, in the case of tensile failure, using a G_{f1} based linear softening constitutive relation (Figure 4), the updated normal tensile stress ($f_{t,T}^{\mathrm{up}}$) is computed as

$$\begin{aligned} f_{t,T}^{\mathrm{up}} &= \delta_t f_{t,T}, \\ \delta_t &= \left(1 - \frac{u_n - f_{t,T}/K_{n,T}}{2G_{f1,T}/f_{t,T} - f_{t,T}/K_{n,T}}\right), \end{aligned} \tag{12}$$

where u_n represents the current normal contact displacement and $G_{f1,T}$ represents the temperature-dependent mode-1 fracture energy. For the considered linear shear softening as depicted in Figure 4, the ultimate shear displacement at the contact point is computed as

$$\begin{aligned} u_s^l &= \frac{2G_{f2,T}}{\tau_T^{\max} - \tau_T^{\mathrm{res}}} + \frac{\tau_T^{\mathrm{res}}}{K_{s,T}}, \\ \tau_T^{\max} &= c_T^o + \sigma_n \tan\phi_T^o;\ \tau_T^{\mathrm{res}} = c_T^{\mathrm{res}} + \sigma_n \tan\phi_T^{\mathrm{res}}, \end{aligned} \tag{13}$$

where $G_{f2,T}$ represent the mode-2 fracture energy, c_T^{o} and c_T^{res} represent temperature-dependent initial and residual cohesion, ϕ_T^{o} and ϕ_T^{res} represent temperature-dependent initial and residual friction angle. At a given temperature T, in the case of shear failure, the updated shear stress ($f_{s,T}^{\mathrm{up}}$) is calculated for the considered softening constitutive relation as follows

$$
\begin{aligned}
c_T^{\mathrm{up}} &= c_T^{\mathrm{o}} + (c_T^{\mathrm{o}} - c_T^{\mathrm{res}})\left(\frac{u_s - \tau_T^{\max}/K_{s,T}}{\tau_T^{\max}/K_{s,T} - u_s^l}\right), \\
\tan(\phi_T^{\mathrm{up}}) &= \tan(\phi_T^{\mathrm{o}}) + \left(\tan(\phi_T^{\mathrm{o}}) - \tan(\phi_T^{\mathrm{res}})\right)\left(\frac{u_s - \tau_T^{\max}/K_{s,T}}{\tau_T^{\max}/K_{s,T} - u_s^l}\right), \\
f_{s,T}^{\mathrm{up}} &= \underbrace{\left(\frac{c_T^{\mathrm{up}} + \sigma\tan(\phi_T^{\mathrm{up}})}{\tau_T^{\max}}\right)}_{\delta_s}\tau_T^{\max}.
\end{aligned}
\tag{14}
$$

In the case of compression regime, a bi-linear constitutive behaviour is considered, where the temperature-dependent contact stiffness is computed as

$$
K_{n,T} = \begin{cases} K_{n,T}; \text{if } |u_{n,T}| \le u_{nl,T}, \\ \beta K_{n,T}; \text{if } |u_{n,T}| > u_{nl,T}, \end{cases}
\tag{15}
$$

where β is the hardening stiffness factor, $u_{nl,T}$ is the limiting compressive elastic displacement which is given by $u_{nl,T} = f_{cm,T} / K_{n,T}$. Here $f_{cm,T}$ is the temperature-dependent limiting compressive elastic stress.

2.3 Meso-scale concrete morphology

The preliminary step prior to meso-scale DEM modelling of concrete is random generation of coarse aggregates followed by filling up the spaces between them with cement matrix. Such a random generation of the aggregates-matrix structure must comply with the statistical aspects of the material and should be potentially isotropic at the macro-scale [41]. This can be achieved with the aid of a Monte-Carlo simulation based approach called '*take-and-place method*' and such an approach has been successfully implemented in the past (e.g. [42,43]). It essentially involves three steps. Firstly, the appropriate particle size distribution chart needs to be chosen. In this study, Fuller's gradation curve is chosen, which is one of the most widely accepted particle sized distribution curves for concrete.

The mathematical form of Fuller's gradation curve is given by

$$P(d) = 100\left(\frac{d}{d_{\max}}\right)^{nf} \tag{16}$$

where $P(d)$ represents cumulative percentage passing for a given sieve size d, d_{max} is the maximum aggregate size, and nf is an exponent in the range 0.45-0.7 (nf is adopted as 0.45 in this study). For a maximum coarse aggregate size of 32 mm, the Fuller´s curve is shown in Figure 5, and it is observed to reasonably within the bounds of limiting gradation curves of aggregates corresponding to concrete as given in EN 12620 [44].

In the second step with the volume fraction of coarse aggregate as input, the volume of aggregates in the discrete size intervals ranging from $d_{\min}$ to $d_{\max}$ is generated. Coarse aggregates, in general, correspond to particle size greater than 4.75mm, with volume fraction ranging in general between 0.3-0.5 of the total volume of the concrete. Subsequently, within each size interval, aggregates of various sizes are generated randomly from the Fuller´s gradation curve. For the present 2D meso-scale simulation, aggregates are initially idealized as circular inclusions for the above random generation. Such a 2D meso-scale morphology does not precisely account for stereo-metric relations, as in the case of the 3D model. However, it is reasonably accurate in predicting the macroscopic behaviour of concrete and its corresponding fracture mechanisms at the meso-scale level and has been successfully implemented in the past (e.g. [43,45]). In the last step, the generated aggregate entities are placed in the overall volume of concrete, such that it satisfies no overlapping between aggregates. Detailed algorithmic implementation of the take-and-place method can be seen in [42]. In the present study, utilizing the random distribution of circular-shaped aggregates, the meso-scale 2D DEM model is generated with the polyhedral blocks in the following sequence. Firstly, the concrete specimen is discretized with the polyhedral blocks. Next, the previously obtained geometrical data pertaining to the random distribution of aggregates is superimposed on the DEM model and

the material properties of the intersected zones, and corresponding contacts are changed accordingly. The procedure for generating meso-scale concrete morphology using the present polyhedral block-based DEM modelling is schematically shown in Figure 6. DEM analysis on such morphology is demonstrated in Section 3 and Section 4, corresponding to room temperature and elevated temperatures, respectively.

3 Uniaxial compression test simulation on concrete at room temperature

This section presents the validation of the developed DEM framework against the experimental observations corresponding to room temperature. Anderberg and Thelandersson [2] performed a detailed experimental campaign on concrete at steady-state and transient heating conditions, respectively. Utilizing the developed framework, discontinuum simulation of uniaxial compression failure in concrete is performed at the room temperature, and is compared against the experimental results, of Anderberg and Thelandersson [2], corresponding to room temperature. A cylindrical concrete sample of size 150 mm diameter and 300 mm height is idealized as 2D plane stress model (150 300 mm^2). For the given concrete geometry, DEM discretization is performed with 5000 polyhedral blocks, and the previously discussed take-and-place algorithm is applied. Further, each polyhedral block is divided into approximately five tetrahedral zones. The statistical aspects of the morphology of concrete are depicted in Figure 7. Aggregate geometry generation by the Monte Carlo based take-and-place algorithm followed by its superimposition on the DEM discretization has resulted in a DEM model as shown in the same figure. It is to be noted that such a superimposition has resulted in a coarse aggregate volume fraction of 0.31 in the DEM model against the input volume fraction of 0.34. Further, the shape of the aggregates is non-circular, which might result in different stress states as well compared to that of circular aggregates morphology. These limitations are due to the chosen geometry generation algorithm within the present 3DEC software framework.

The sample is subjected to compressive loads applied through the top with a fixed velocity boundary condition, whereas the bottom steel plate is fixed during the analysis.

Initially, the discrete meso-models are subjected to self-weight and the DEM analysis is performed till equilibrium is attained under gravity. Next, a displacement rate (velocity) of 0.8 mm/sec, in the downward direction, is applied on the upper steel plate. The reaction forces are extracted at each time step via the implemented subroutine in the software, using FISH functions.

3.1 Model parameters

The macro-scale uniaxial response of concrete is governed by the meso-scale properties pertaining to the zones and contact parameters of the meso-model. In the current uniaxial simulation, these properties are chosen in an iterative process, to obtain the macroscopic parameters as given in [2,13]. These include the elastic modulus (E=21.5 GPa), compressive strength (f_c=35 MPa) and the inelastic strain at peak (ε_{ic} =0.0015). The elastic properties of the aggregates and cement matrix defined for the zones are shown in Table 1. The steel plate is replicated as a single continuum block with E=200 GPa and υ=0.3.

In case of the contact points, the normal (K_n) and the tangential stiffness (K_s) are calculated from the elastic properties of aggregates and cement mortar, respectively, using the relation given below, similar to [46].

$$K_n = \frac{E}{t_b}, \qquad K_s = \frac{G}{t_b}, \tag{17}$$

where t_b is the average thickness of the fracture zone which is 1.6 mm for the sample size of 5000 blocks. As discussed in Section 2, the mechanical parameters of contact points of the aggregate mortar interface (A-M) are lumped with that of ITZ. Their inherently lower strength

and stiffness compared to that of cement mortar is considered in the proposed numerical models by considering 80% of strength and stiffness to that of the mortar-mortar interface (M-M). Furthermore, in the present study, previously mentioned 2D plane stress conditions in a 3D polyhedral DEM modelling strategy is simulated by setting the Poisson's ratio in z-direction equivalent to zero, in addition to restrained displacement in z-direction over the entire model.

Table 2 details the mechanical parameters of the contacts belonging to various joints. In the purview of the present study, precise macro-scale model predictions can be obtained by choosing the relevant meso-scale contact parameters, which are detailed in Section 2.2 However, experimental data at such a scale is rather scarce. This limitation can be partly addressed from the DEM based multi-scale mechanical correlation studies available in the literature (e.g., [40,47]) which correlates the meso-level contact parameters to the macro mechanical response. The tensile strength of the M-M interface is taken as 2.5 MPa, and the tensile fracture energy (G_{f1}) is taken as 60 N/m from the studies of Rots [48]. In case of compression, f_{cm} is taken as 33 MPa, whereas β is taken as 0.05 for the M-M interface. In the case of shear, due to the lack of data, the cohesion (c_o) in M-M interface is taken as 1.5 times the tensile strength as given in [40,47]. The shear fracture energy (G_{f2}) is taken as four times the tensile fracture energy (G_{f1}) as in [47]. The normal stiffness of the contact points between the concrete sample and steel plate is taken as for the M-M interface 18400 GPa/m and a frictionless behaviour is considered in the tangential direction.

3.2 Results and discussion

For the considered, target macro-mechanical response parameters given in [2,13] (E=21.5 GPa, f_c=35 MPa and ε_{ic} =0.0015), the obtained values from the DEM analysis are summarized in Table 3. Further, the macro-scale stress-strain curve obtained from the DEM analysis is compared against the experimental predictions of Anderberg and Thelandersson [2]

corresponding to the room temperature, as shown in Figure 8. The results indicate that the developed discrete meso-model is reasonably accurate in predicting the macro-scale uniaxial compression response of concrete. Moreover, the failure patterns at the designated stress states pointed out in Figure 8 as red circles are separately shown in Figure 9. The explicit representation of the concrete morphology provides an opportunity to examine the complex stress distribution among each constituent of concrete through contact points, which are governed by the respective failure modes. For instance, as shown in Figure 8, in the case of the hardening part, the overall macroscopic behaviour is predominantly governed by the bi-linear contact constitutive model in compression. Later, the overall behaviour is governed by the tensile failure and shear sliding at the contact points. This is evident in Figure 9, at peak stress point B, where the predominant micro-cracks due to shear rupture and a few normal separation cracks near the loading plate are present.

In the softening regime (Figure 9c, point C), these micro-cracks develop further into macro-cracks by the dissipation of tensile and shear fracture energies, respectively.

4 Transient heating of concrete under various compressive stresses

As mentioned in Section 3, Anderberg and Thelandersson [2] and Thelanderssom [13,49] performed detailed thermo-mechanical characterization tests to understand the thermo-mechanical strain and its components in concrete. These tests include a) constant temperature and constant load tests for characterizing isothermal creep, b) heating the sample till steady-state temperature followed by loading, and c) loading the sample initially followed by heating till failure under the sustained mechanical loading. In the loading followed by heating tests, the total thermo-mechanical strain in concrete is quantified at various initial compression stress levels. In such tests, the concrete sample was initially compressed at various stress levels ($\sigma/f_{c,25}$=0, 0.225, 0.445, 0.675), and later the sample was heated till failure. For the discrete

meso-model pertaining to our sample, such thermo-mechanical loading conditions are simulated.

It is worth to note that in the experimental investigation by Anderberg and Thelandersson [2], a heating rate up to 5 ˚C/min is considered, and their experimental campaign has reported that such low heating rate resulted in a relatively uniform temperature distribution for their chosen sample size (75 ×150 mm). This condition is artificially simulated in the present DEM based thermo-mechanical simulation by modifying the obtained transient profiles of the thermal analysis within the DEM framework to be uniform over the sample. It should be mentioned that such simplification taken from the experimental campaign of Anderberg and Thelandersson [2] is still physically imprecise due to the possibility of the presence of microthermal gradients at the boundaries which might slightly influence the model predictions. However, such an approach is chosen due to the lack of thermophysical properties at the meso-scale level (aggregates, cement mortar and ITZ) corresponding to their experimental data. Subsequently, transient thermo-mechanical analysis as discussed in Section 2.2 is performed with those thermal profiles in conjunction with the temperature-dependent model parameters.

4.1 Model parameters

For the transient thermo-mechanical DEM simulation, temperature-dependency is applied to the calibrated contact and zone properties given in Table 1 and Table 2 of Section 3.1, corresponding to the room temperature. It is to be noted that at the meso-scale, very limited data is available in the literature to establish the temperature-dependency in the zone and contact parameters. Accordingly, relevant assumptions and idealizations have been made to facilitate the model predictions. Figure 10 shows the considered temperature-dependency in elastic modulus (aggregates and cement mortar) and compressive strength (cement mortar and aggregates).

In the case of cement mortar, the temperature-dependency in elastic modulus and compressive strength are chosen from the work of Harmathy [50]. Moreover, in the case of aggregates, the temperature-dependency as in concrete is assumed from the work of Anderberg and Thelandersson [2], due to the lack of comprehensive experimental data. It is necessary to note that cement mortar exhibit initial thermal dilation followed by thermal contraction while heating, whereas aggregates exhibit thermal dilation during heating [51,52]. Figure 11 depicts such phenomena, which is taken from the experimental thermal strain characterization study of Cruz and Gillen [52] on cement mortar and dolomite aggregate. Considering these phenomena in conjunction with the overall thermal expansion coefficients of concrete available in the literature (e.g. [53]), the following mathematical forms are considered for thermal expansion coefficients and are given by

$$\begin{aligned} \alpha_{\mathrm{A}} &= \eta_1 + \eta_2 T, \\ \alpha_{\mathrm{M}} &= \zeta_1 - \zeta_2 T^2, \end{aligned} \tag{18}$$

where α_{A} and α_{M} represent the thermal expansion coefficients of aggregates and cement mortar, respectively. The coefficients (η_1=9×10^{-6}; η_2=7×10-8, ζ_1=9×10^{-7} and ζ_2=6×10^{-11}) are chosen in an iterative process to fit the transient thermo-mechanical DEM simulation pertaining to zero loading level ($\sigma/f_{c,25}$=0).

The normal and shear contact stiffnesses are computed using Equation (17), with temperature-dependent elastic modulus. Due to the lack of experimental data, the temperature dependency in tensile strength of mortar is assumed to be same as that of compressive strength. Additionally, the model parameter correlation between ITZ and cement mortar, as discussed in Section 3.1, is assumed to exist in the same way at elevated temperatures as well. The fracture energies (G_{f1} and G_{f2}), given in Table 2, are taken and the temperature-dependency as in $f_{t,T}$ is applied with constant ultimate failure strain (see [54]). As in the case of room temperature, c_T^{res}

is assumed to be 1.5 times that of $f_{t,T}$. Further, due to the lack of experimental data, no degradation is considered in the friction angles.

4.2 Results and discussion

The results obtained from discrete meso-models are compared against the experimental values of Thelandersson [49], as shown in Figure 12. The results indicate that the developed meso-scale DEM model is reasonably accurate in predicting the transient thermo-mechanical behaviour of concrete. In Figure 12, the deviation of the experimental results with an increase of initial stress level ($\sigma/f_{c,25}$) can be clearly observed. This is attributed to the thermo-elastic zone constitutive model, which does not account for other critical phenomena (e.g C-S-H gel disintegration coupled with moisture transport) that contribute to the LITS. The fracture patterns of the computational models at various initial stress levels ($\sigma/f_{c,25}$=0, 0.225, 0.445, 0.675) are shown in Figure 13, Figure 14, Figure 15 and Figure 16, respectively. Different fracture mechanisms are observed due to the thermo-mechanical loading that is governed by the combined effect of: a) differential thermal expansion between aggregates and cement mortar, and b) applied load. As in the case of zero initial stress condition ($\sigma/f_{c,25}$=0), with the increase in temperature beyond 300 ˚C, the effects of differential thermal expansion are predominant. Due to such phenomena, non-uniform lateral expansion is observed. Further, it resulted in shear rupture, and normal separation cracks sparsely distributed over the entire sample (Figure 13, T=600 ˚C).

With the further increase in temperature, bridging between those cracks is observed, as they are further distributed over the sample (Figure 13, T=800 ˚C).

Due to the applied initial compression loading, at room temperature, the contact points are subjected to compression, shear and tensile stress states. With further loading, as discussed in Section 3.2, micro-cracks of tension and shear mode originate and evolve into a macro cracking

mechanism. In case of transient heating as observed here, the initial micro-cracks due to the differential thermal expansion govern the fracture pattern evolution with temperature, in conjunction with the applied loading and temperature-dependent material degradation and damage. Such combined phenomena result in macro-cracks with further release of fracture energy and eventually bridging between macro-cracks.

For instance, as in the case of $\sigma/f_{c,25}$= 0.225 (Figure 14) and $\sigma/f_{c,25}$= 0.445 (Figure 15), with temperature increase, micro-cracks are formed over the concrete morphology (T < 400˚ C). It is to be noted that the micro-cracks are relatively well distributed over the sample in the case of $\sigma/f_{c,25}$= 0.225 (Figure 14) and $\sigma/f_{c,25}$= 0.445 (Figure 15), compared to that of $\sigma/f_{c,25}$= 0.675 (Figure 16). This is attributed to the higher initial compressive loading which reduces the contact sliding and separation due to differential thermal expansion to a certain extent. With an increase in temperature, such micro-cracks further developed with additional release of fracture energy (Figure 14, T=500 ˚ C and Figure 15, T=400 ˚ C). Eventually, these cracks developed into macro-cracks and eventually lead to sample failure. In the case of $\sigma/f_{c,25}$= 0.225 (Figure 14) and $\sigma/f_{c,25}$= 0.445 (Figure 15), the macro-cracks at failure are located in the vicinity of A-M interface and such cracks are well distributed over the sample.

Moreover, these cracks have resulted in an overall axial-split mode of fracture at the failure temperature. In the case of $\sigma/f_{c,25}$= 0.675 (Figure 16, T=400 ˚ C), the macro-cracks at failure are relatively less compared to the other loading cases. Furthermore, these cracks are predominantly located near the aggregate mortar interface, and near the loading plates. Still, an overall axial-split mode of failure is observed in this loading case as well.

5 Conclusions

In this research, the mechanical and thermo-mechanical behaviour of concrete, together with the associated fracture mechanisms, are analyzed based on the discrete element method. The proposed modelling strategy is referred to as discrete meso modelling, where a system of deformable blocks, discretized into zones, is employed so that the blocks can interact with each other through their contact points. To achieve a random and explicit representation of concrete morphology at the meso-scale, a Monte Carlo based algorithm is utilized to generate aggregates and cement mortar. The interface transition zone between the aggregate and mortar is considered separately, and its properties are lumped at the aggregate-mortar joints. The developed modelling strategy addresses thermal dilation and temperature-dependent material degradation, as well as the damage progression with the aid of zone and implemented contact constitutive models. In particular, thermo-elasticity constitutive model for zones and fracture energy-based temperature-dependent failure envelopes for contacts are utilized through this study. The developed computational framework is validated using experimental observations, both at room temperature and transient heating conditions, where the numerical models are line with the experimental results.

Critical physical phenomena, including the evolution of the micro and macro cracking patterns under various temperatures due to differential thermal expansion in the concrete constituents and effect of initial load level, are intricately examined. The results indicate that the cracking pattern evolution with temperature is mainly governed by the differential thermal expansion phenomenon in conjunction with the initial load level. Given the detailed mesoscopic discontinuum modelling capabilities, the present framework can be utilized for potential applications which include: a) detailed thermo-mechanical characterization of various kinds of concrete, b) understanding the evolution of fracture patterns in concrete under thermo-mechanical loading c) sensitivity analyses, and d) post-heating residual capacity quantification

studies. Moreover, the future work will focus on a) extending this framework to 3D, with precise morphology b) improvised material models for relatively accurate thermo-mechanical predictions, and c) incorporation of spalling phenomena in the proposed framework.

6 Acknowledgements

The first author would like to acknowledge the post-doctoral fellowship offered by the University of Minho for this research. This work was partly supported by UID/ECI/04029/2019 - ISISE, funded by national funds through the FCT/MCTES (PIDDAC).

7 References

[1] T.C. Hansen, L. Eriksson, Temperature Change Effect on Behavior of Cement Paste, Mortar, and Concrete Under Load, ACI J. Proc. 63 (1966) 489–504. https://doi.org/10.14359/7635.

[2] Y. Anderberg, S. Thelandersson, Stress and deformation characteristics of concrete at high temperatures. Experimental investigation and material behaviour model, Lund Institute of Technology, Lund University, Sweeden, 1976.

[3] G.A. Khoury, B.N. Grainger, P.J.E. Sullivan, Transient thermal strain of concrete: literature review, conditions within specimen and behaviour of individual constituents, Mag. Concr. Res. 37 (1985) 131–144. https://doi.org/10.1680/macr.1985.37.132.131.

[4] J.C. Mindeguia, I. Hager, P. Pimienta, H. Carré, C. La Borderie, Parametrical study of transient thermal strain of ordinary and high performance concrete, Cem. Concr. Res. 48 (2013) 40–52. https://doi.org/10.1016/j.cemconres.2013.02.004.

[5] G. Torelli, P. Mandal, M. Gillie, V.X. Tran, Concrete strains under transient thermal conditions: A state-of-the-art review, Eng. Struct. 127 (2016) 172–188. https://doi.org/10.1016/j.engstruct.2016.08.021.

[6] V. Kodur, Properties of Concrete at Elevated Temperatures, ISRN Civ. Eng. 2014 (2014) 468510. https://doi.org/10.1155/2014/468510.

[7] Z.P. Baănt, W.J. Raftshol, Effect of cracking in drying and shrinkage specimens, Cem. Concr. Res. 12 (1982) 209–226. https://doi.org/10.1016/0008-8846(82)90008-4.

[8] H. Colina, J. Sercombe, Transient thermal creep of concrete in service conditions at temperatures up to 300°C, Mag. Concr. Res. 56 (2004) 559–574. https://doi.org/10.1680/macr.2004.56.10.559.

[9] L. Bisby, A. Chair, H. Mostafaei, State-of-the-Art on Fire Resistance of Concrete Structure Structure-Fire Model Validations, NIST-Special Publications: International R&D Road Map for Fire Resistance of Structures., 2014.

[10] U. Schneider, Concrete at High Temperatures-A General Review, Fire Saf. J. 13 (1988) 55–68.

[11] J. Cai, I. Burgess, R. Plank, A generalised steel/reinforced concrete beam-column element model for fire conditions, Eng. Struct. 25 (2003) 817–833.

[12] G. Srivastava, P.R. Prakash, An integrated framework for nonlinear analysis of plane frames exposed to fire using the direct stiffness method, Comput. Struct. 190 (2017) 173–185.

[13] S. Thelandersson, ON THE MULTIAXIAL BEHAVIOUR OF CONCRETE EXPOSED TO HIGH TEMPERATURE., in: Trans. Int. Conf. Struct. Mech. React. Technol., 1983.

[14] C. Yu, Z. Huang, I.W. Burgess, R.J. Plank, Development and validation of 3{D} composite structural elements at elevated temperatures, J. Struct. Eng. 136 (2010) 275–284.

[15] C.E. Majorana, V.A. Salomoni, G. Mazzucco, G.A. Khoury, An approach for modelling concrete spalling in finite strains, Math. Comput. Simul. 80 (2010) 1694–1712. https://doi.org/10.1016/j.matcom.2009.05.011.

[16] Y. Yao, K. Wang, X. Hu, Thermodynamic-Based Elastoplasticity Multiaxial Constitutive Model for Concrete at Elevated Temperatures, J. Eng. Mech. 143 (2017) 04017039. https://doi.org/10.1061/(ASCE)EM.1943-7889.0001250.

[17] R. De Borst, L.J. Sluys, H.B. Mühlhaus, J. Pamin, Fundamental issues in finite element analyses of localization of deformation, Eng. Comput. 10 (1993) 99–121. https://doi.org/10.1108/eb023897.

[18] P.A. Cundall, Formulation of a three-dimensional distinct element model—Part I. A scheme to detect and represent contacts in a system composed of many polyhedral blocks, Int. J. Rock Mech. Min. Sci. Geomech. 25 (1988) 107–116.

[19] M. Obermayr, K. Dressler, C. Vrettos, P. Eberhard, A bonded-particle model for cemented sand, Comput. Geotech. 49 (2013) 299–313. https://doi.org/10.1016/j.compgeo.2012.09.001.

[20] L. Daudeville, E. Buzaud, F. Dupray, Y. Malecot, L. Daudeville, E. Buzaud, A mesoscopic model for the behaviour of concrete under high confinement, Int. J. Numer. Anal. METHODS Geomech. Int. J. Numer. Anal. Meth. Geomech. 33 (2009) 1407–1423. https://doi.org/10.1002/nag.771.

[21] I. Carol, C.M. López, O. Roa, Micromechanical analysis of quasi-brittle materials using fracture-based interface elements, Int. J. Numer. Methods Eng. 52 (2001) 193–215. https://doi.org/10.1002/nme.277.

[22] J. Kozicki, J. Tejchman, Effect of aggregate structure on fracture process in concrete using 2D lattice model, Arch. Mech. 59 (2007) 365–384.

[23] J.E. Bolander, B.D. Le, Modeling crack development in reinforced concrete structures under service loading, Constr. Build. Mater. 13 (1999) 23–31.

[24] A. Fascetti, J.E. Bolander, N. Nisticó, Lattice discrete particle modeling of concrete under compressive loading: Multiscale experimental approach for parameter determination, J. Eng. Mech. 144 (2018) 1–11. https://doi.org/10.1061/(ASCE)EM.1943-7889.0001480.

[25] S. Sinaie, A. Heidarpour, X.L. Zhao, A micro-mechanical parametric study on the strength degradation of concrete due to temperature exposure using the discrete element method, Int. J. Solids Struct. 88–89 (2016) 165–177. https://doi.org/10.1016/j.ijsolstr.2016.03.009.

[26] P. Grassl, C. Pearce, Mesoscale approach to modeling concrete subjected to thermomechanical loading, J. Eng. Mech. 136 (2010) 322–328. https://doi.org/10.1061/(ASCE)0733-9399(2010)136:3(322).

[27] Itasca Consulting Group Inc., 3DEC Three Dimensional Distinct Element Code, (2013).

[28] B. Pulatsu, E. Erdogmus, P.B. Lourenço, R. Quey, Simulation of uniaxial tensile behavior of quasi-brittle materials using softening contact models in DEM, Int. J. Fract. 217 (2019) 105–125. https://doi.org/10.1007/s10704-019-00373-x.

[29] R. Quey, Neper Reference Manual 3.5.1, (2014).

[30] R. Quey, L. Renversade, Optimal polyhedral description of 3D polycrystals: Method and application to statistical and synchrotron X-ray diffraction data, Comput. Methods Appl. Mech. Eng. 330 (2018) 308–333. https://doi.org/10.1016/j.cma.2017.10.029.

[31] B. Pulatsu, S. Kim, E. Erdogmus, P.B. Lourenço, Advanced analysis of masonry retaining walls using mixed discrete-continuum approach, Proc. Inst. Civ. Eng. - Geotech. Eng. (2020) 1–34. https://doi.org/10.1680/jgeen.19.00225.

[32] B. Pulatsu, E. Erdogmus, P.B. Lourenço, J. V. Lemos, K. Tuncay, Numerical modeling of the tension stiffening in reinforced concrete members via discontinuum models, Comput. Part. Mech. (2020). https://doi.org/10.1007/s40571-020-00342-5.

[33] K.L. Scrivener, A.K. Crumbie, P. Laugesen, The interfacial transition zone (ITZ) between cement paste and aggregate in concrete, Interface Sci. 12 (2004) 411–421. https://doi.org/10.1023/B:INTS.0000042339.92990.4c.

[34] P. Mondai, S.R. Shah, L.D. Marks, Nanoscale characterization of cementitious materials, ACI Mater. J. 105 (2008) 174–179. https://doi.org/10.1007/978-3-319-17088-6_5.

[35] J. Argyris, J. Doltsinis, On the natural formulation and analysis of large deformation coupled thermomechanical problems, Comput. Methods Appl. Mech. Eng. 25 (1981) 195–253.

[36] P.A. Cundall, Distinct element models of rock and soil structure, Anal. Comput. Methods Eng. Rock Mech. (1987) 129–163.

[37] Itasca, 3DEC Universial Discrete Element Code Theory and Background, Minneapolis, 2004.

[38] J. V. Lemos, Block modelling of rock masses. Concepts and application to dam foundations, Rev. Eur. Génie Civ. 12 (2008) 915–949. https://doi.org/10.3166/ejece.12.915-949.

[39] E. Oñate, F. Zárate, J. Miquel, M. Santasusana, M.A. Celigueta, F. Arrufat, R. Gandikota, K. Valiullin, L. Ring, A local constitutive model for the discrete element method. Application to geomaterials and concrete, Comput. Part. Mech. 2 (2015) 139–160. https://doi.org/10.1007/s40571-015-0044-9.

[40] B. Pulatsu, E. Erdogmus, P.B. Lourenço, J. V. Lemos, J. Hazzard, Discontinuum analysis of the fracture mechanism in masonry prisms and wallettes via discrete element method, Meccanica. 55 (2020) 505–523. https://doi.org/10.1007/s11012-020-01133-1.

[41] Z.P. Bazant, Random Particle Model for Fracture of Aggregate or Fiber Composites Multi-Decade Concrete Creep View project Mechanisms-based constitutive modeling View project, Artic. J. Eng. Mech. 116 (1990) 1686–1705. https://doi.org/10.1061/(ASCE)0733-9399(1990)116:8(1686).

[42] P. Wriggers, S.O. Moftah, Mesoscale models for concrete: Homogenisation and damage behaviour, Finite Elem. Anal. Des. 42 (2006) 623–636. https://doi.org/10.1016/j.finel.2005.11.008.

[43] E.A. Rodrigues, O.L. Manzoli, L.A.G. Bitencourt, T.N. Bittencourt, 2D mesoscale model for concrete based on the use of interface element with a high aspect ratio, Int. J. Solids Struct. 94–95 (2016) 112–124. https://doi.org/10.1016/j.ijsolstr.2016.05.004.

[44] EN-12620, Aggregates for Concrete, British Standards, 2013.

[45] X. Wang, A.P. Jivkov, Combined Numerical-Statistical Analyses of Damage and Failure of 2D and 3D Mesoscale Heterogeneous Concrete, Math. Probl. Eng. 2015 (2015). https://doi.org/10.1155/2015/702563.

[46] T. Kazerani, J. Zhao, Micromechanical parameters in bonded particle method for modelling of brittle material failure, Int. J. Numer. Anal. Methods Geomech. 34 (2010) 1877–1895. https://doi.org/10.1002/nag.884.

[47] J. Pina-Henriques, P.B. Lourenço, Masonry compression: A numerical investigation at the meso-level, Eng. Comput. (Swansea, Wales). 23 (2006) 382–407. https://doi.org/10.1108/02644400610661163.

[48] J. Rots, Computational Modelling of Concrete Fracture, Delft University of Technology, 1988.

[49] S. Thelandersson, Modeling of combined thermal and mechanical action in concrete, J. Eng. Mech. 113 (1987) 893–906. https://doi.org/10.1061/(ASCE)0733-9399(1987)113:6(893).

[50] T. Harmathy, J.B.-J. Proceedings, U. 1966, Hydrated Portland Cement and Lightweight Concrete at Elevated

Temperatures, ACI J. Proc. 63 (1966). https://doi.org/10.14359/7616.

[51] Z.P.. BAZANT, M.F. KAPLAN, Concrete at high temperatures - Material properties and mathematical, Addison-Wesley, 1996.

[52] C.R. Cruz, M. Gillen, Thermal expansion of Portland cement paste, mortar and concrete at high temperatures, Fire Mater. 4 (1980) 66–70. https://doi.org/10.1002/fam.810040203.

[53] CEN (European committee for Standardization)," Design of concrete structures. Part 1–2: General rules –Structural Fire Design"., Eurocode-2, Brussels, 2004.

[54] P.R. Prakash, M. Azenha, J.M. Pereira, P.B. Lourenço, Finite element based micro modelling of masonry walls subjected to fire exposure: Framework validation and structural implications, Eng. Struct. 213 (2020) 110545. https://doi.org/10.1016/j.engstruct.2020.110545.

Preprint version, Reference: Patnayakuni RP, Pulatso B, Lourenço PB, Azenha M, Pereira JM (2020), A meso-scale discrete element method framework to simulate thermo-mechanical failure of concrete subjected to elevated temperatures. Engineering Fracture Mechanics, 239, 107269. https://doi.org/10.1016/j.engfracmech.2020.107269

Tables

Table 1. Elastic properties of the zones.

Physical property	**Aggregates**	**Mortar**
Modulus of elasticity (E)	70.0 GPa	29.4 GPa
Poisson's ratio (υ)	0.2	0.2
Shear modulus (G)	29.2 GPa	12.3 GPa

Table 2. Nonlinear contact parameters.

Physical property	**M-M**
K_n (GPa/m)	18400
K_s (GPa/m)	7660
f_t (MPa)	2.5
G_{f1} (N/m)	60
f_{cm} (N/m)	31
β	0.05
c_o (MPa)	3.8
c_{res} (MPa)	$0.01c_o$
ϕ	34 ˚
ϕ_{res}	34 ˚
G_{f2} (N/m)	240

Table 3. Summary of Macro-level DEM model response.

Physical property	**Anderberg and Thelandersson [2]**	**DEM analysis**
E (GPa)	21.5	21.59
f_c (MPa)	35	34.30
ε_{ic}	0.0015	0.00139

Figures

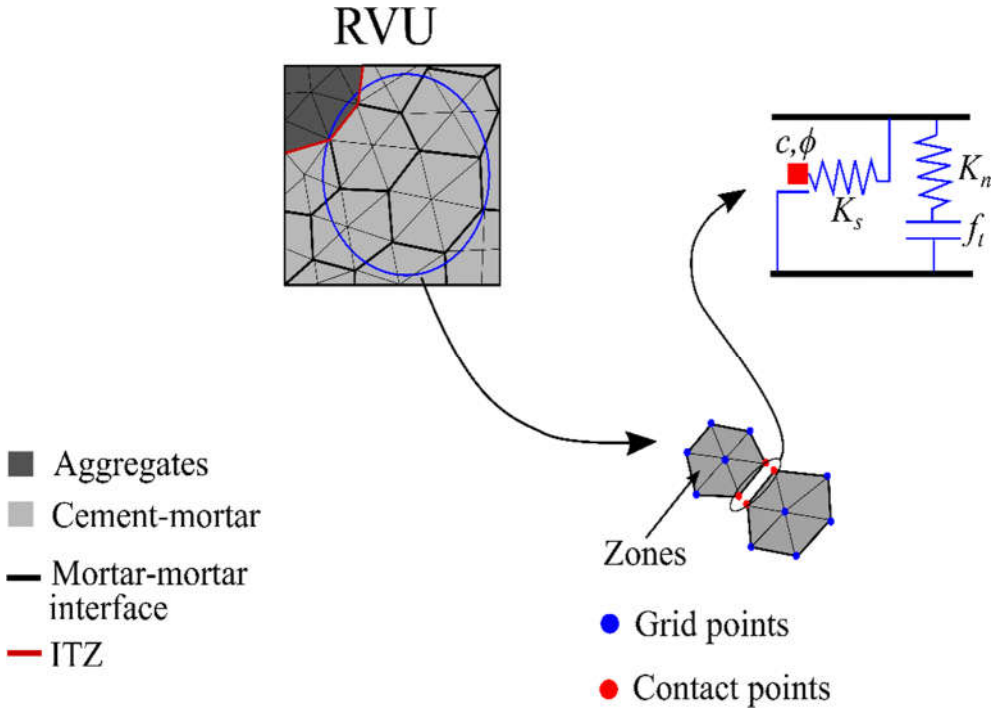

Figure 1. 2D Thermo-mechanical DEM modelling strategy.

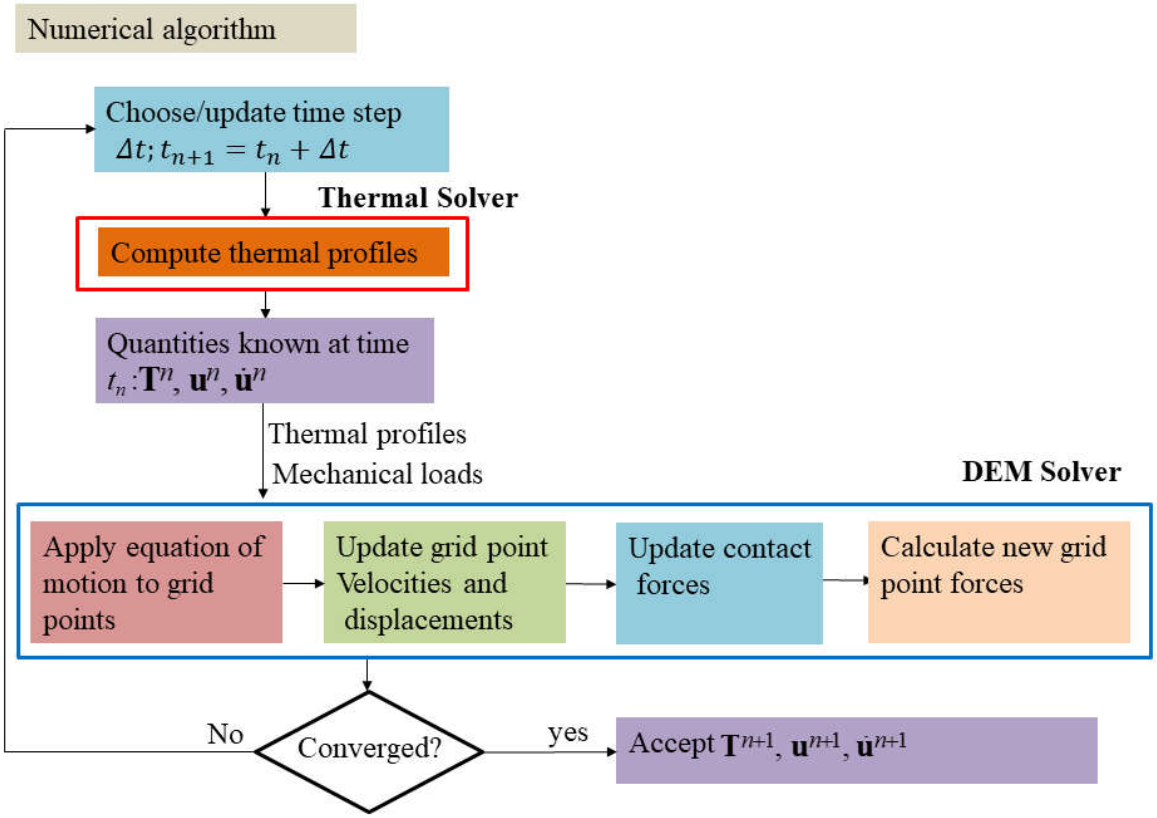

Figure 2. DEM based thermo-mechanical analysis framework.

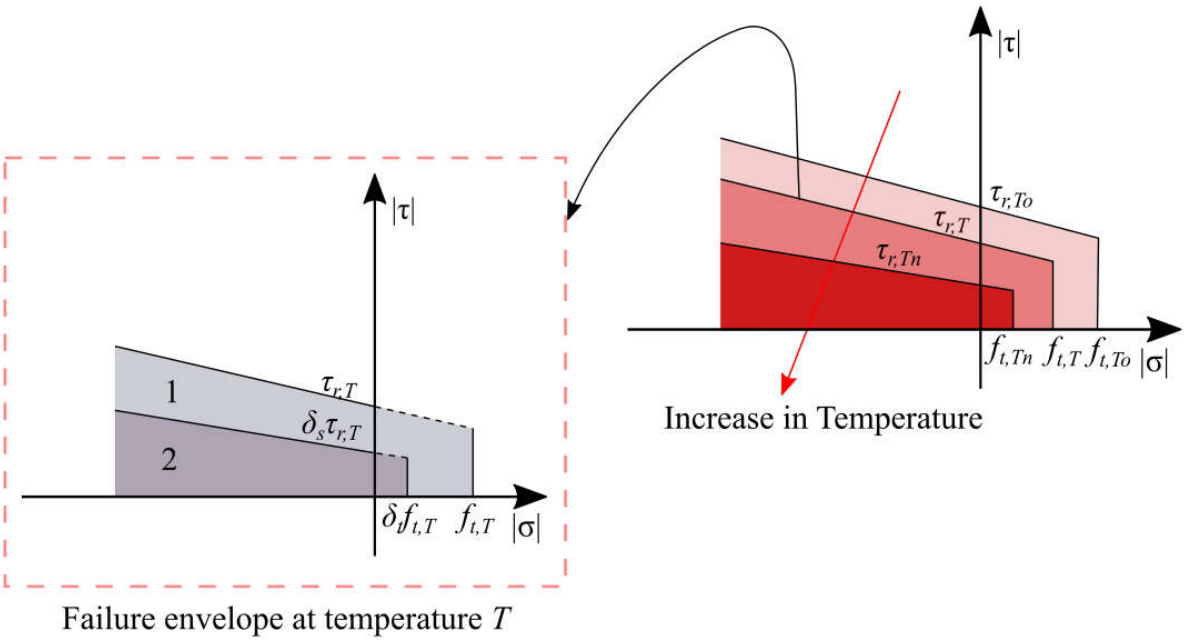

Figure 3: Temperature dependency on interface failure envelopes.

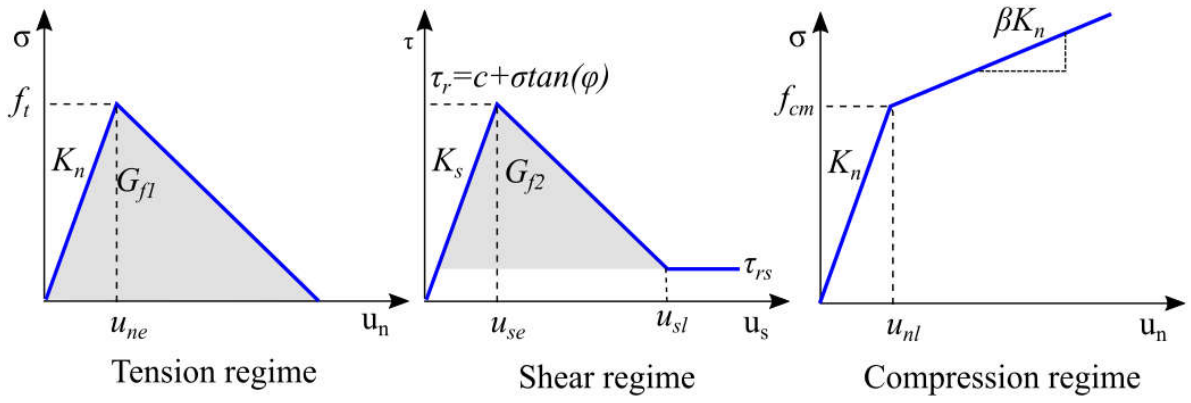

Figure 4. Contact constitutive models in tension, shear, and compression.

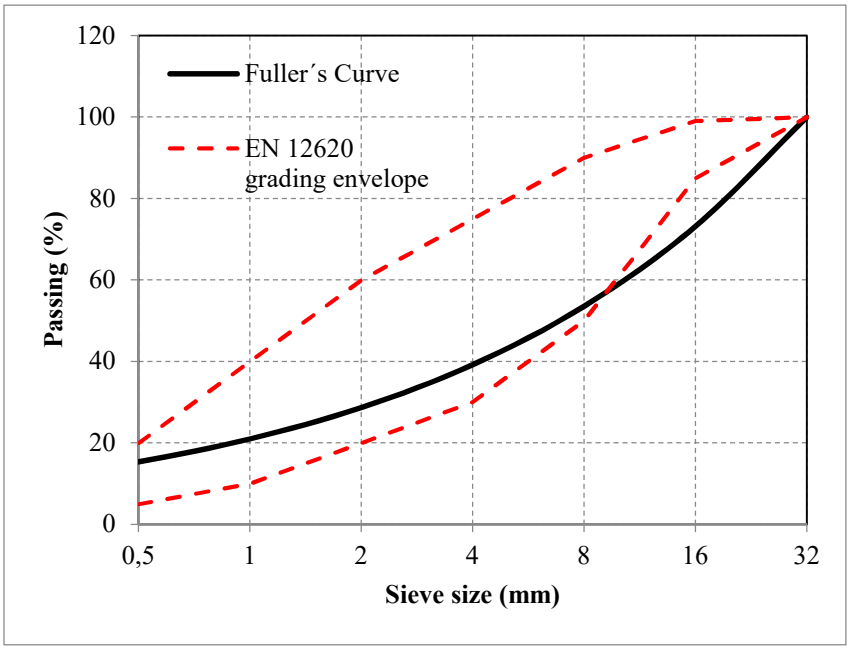

Figure 5: Fuller´s and Limiting gradation curves of aggregates of concrete (EN 12620).

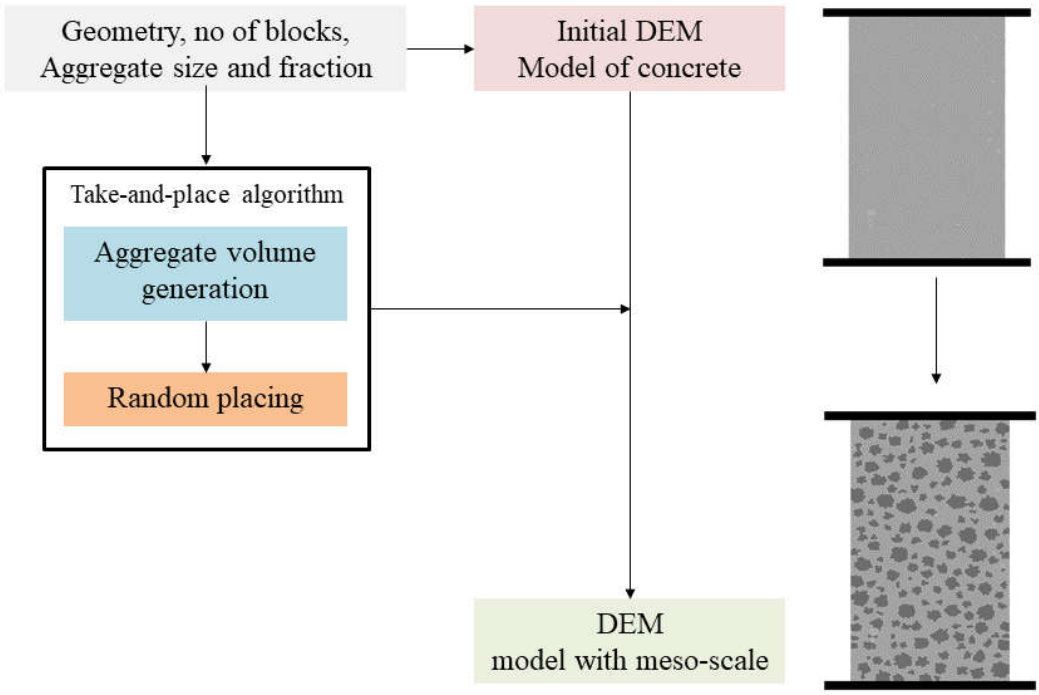

Figure 6. Meso-scale DEM model generation algorithm.

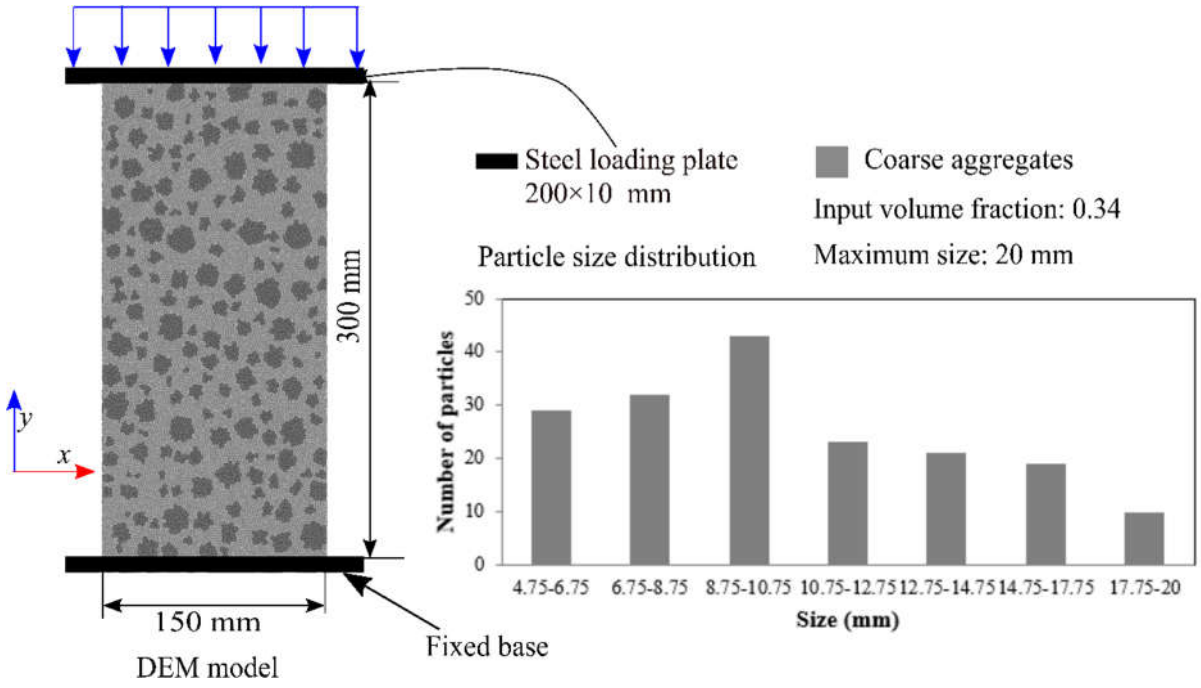

Figure 7. 2D meso-scale DEM model of concrete.

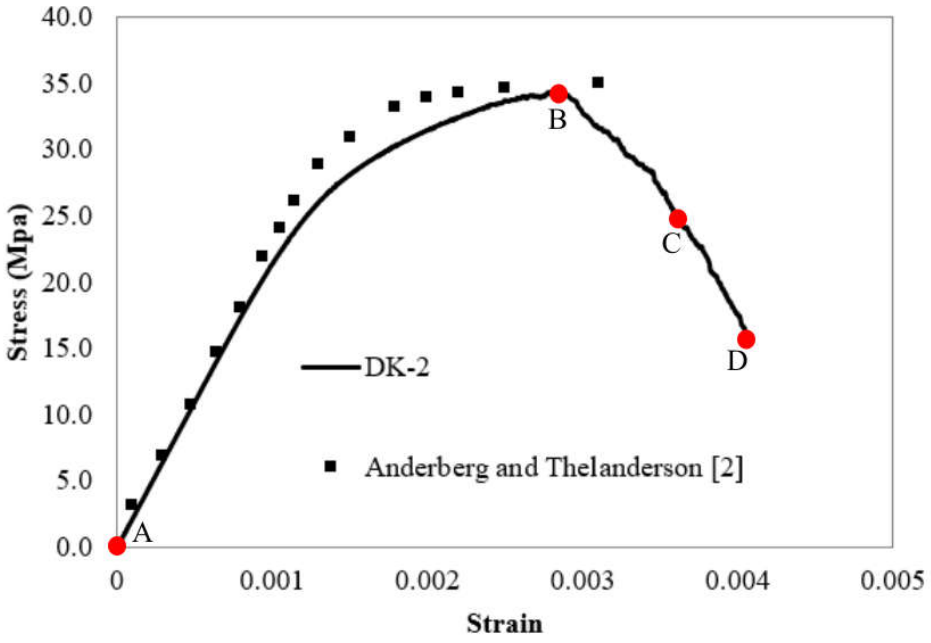

Figure 8. Macro-scale stress-strain response of the DEM model.

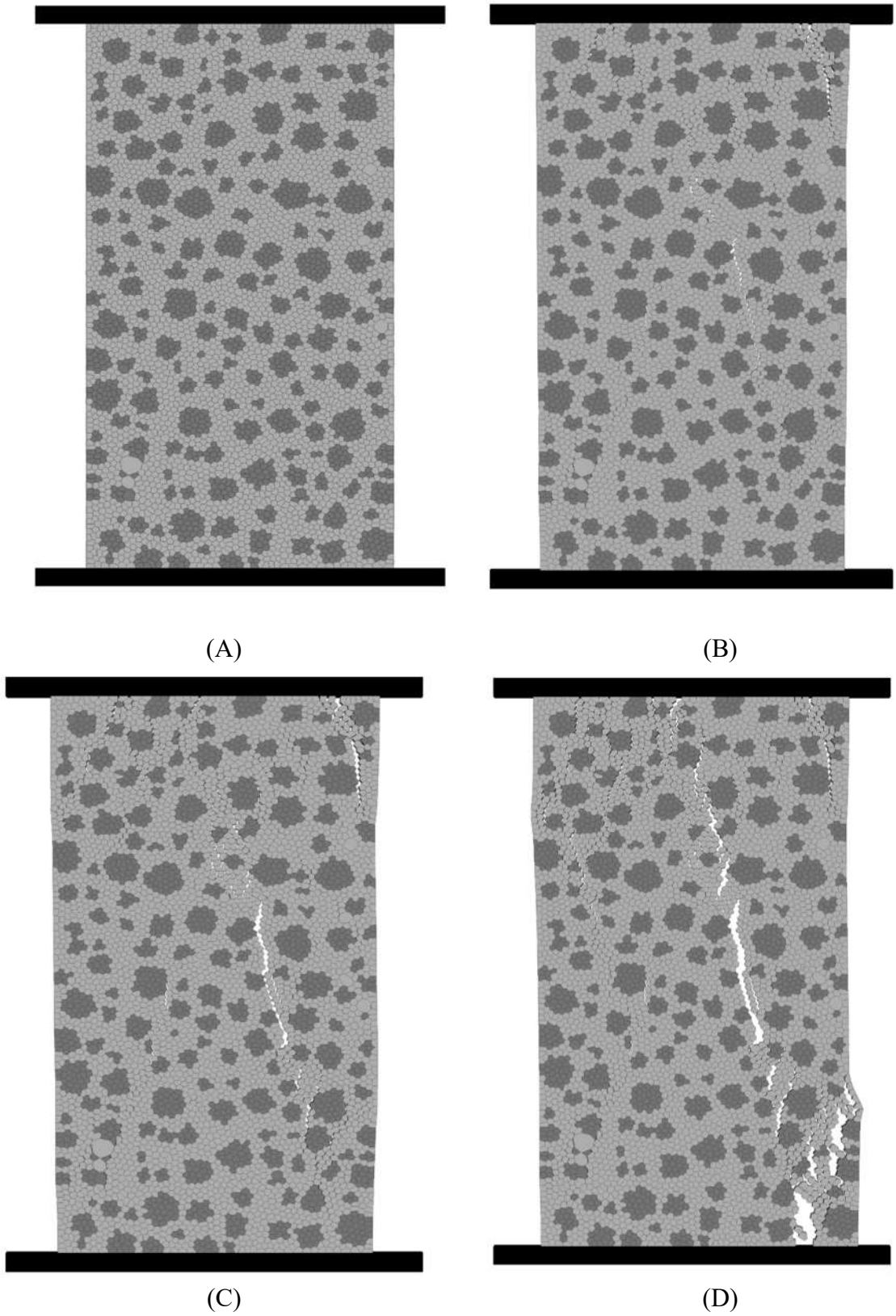

Figure 9. Fracture patterns in uniaxial compression simulation at points A to D identified in Figure 8.

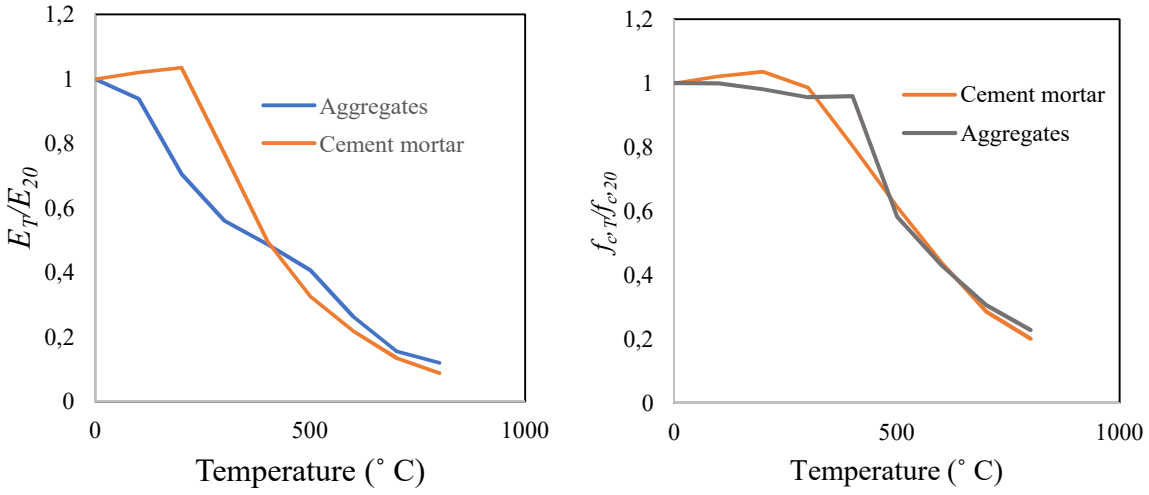

a) Elastic Modulus b) Compressive strength

Figure 10. Adopted temperature-dependent mechanical properties of aggregates [2] and cement mortar [50]**.**

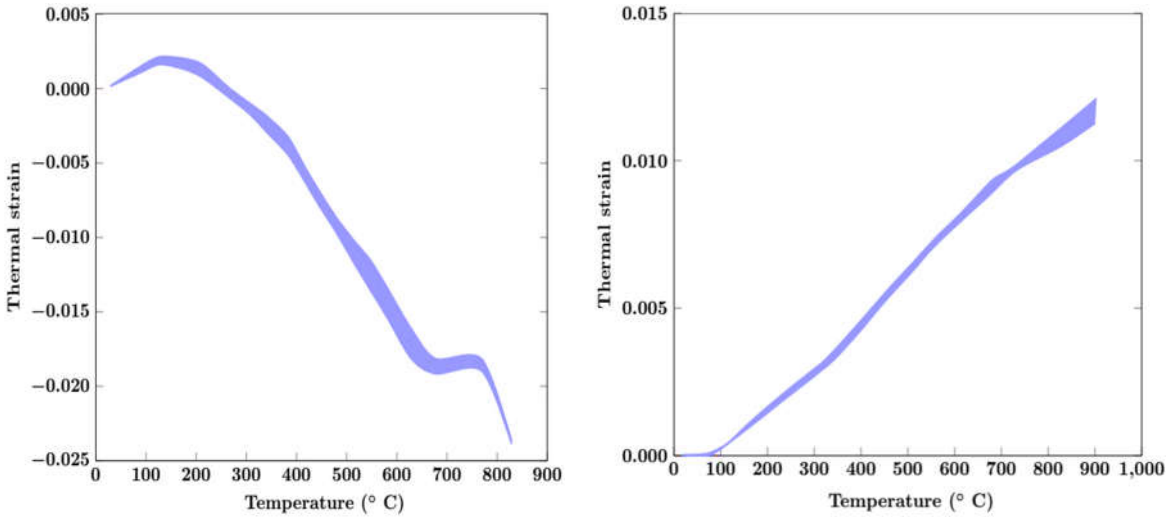

a) Cement Mortar b) Aggregates

Figure 11: Thermal expansion of cement mortar and aggregates [52]**.**

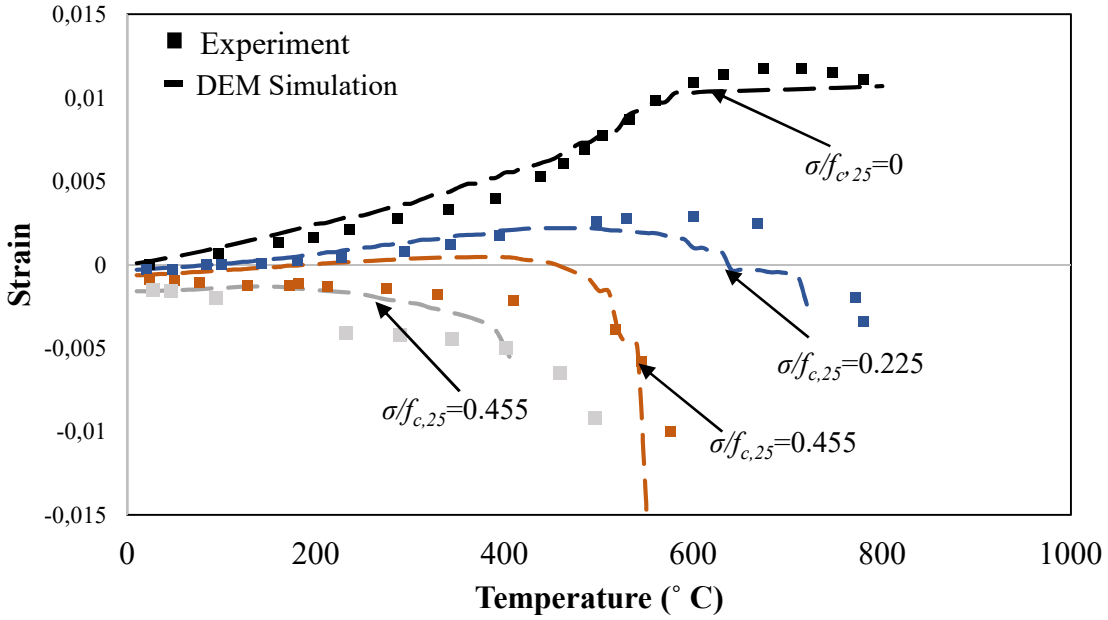

Figure 12. Comparison between experimental and numerical results for temperature vs. total strain under different compressive stresses.

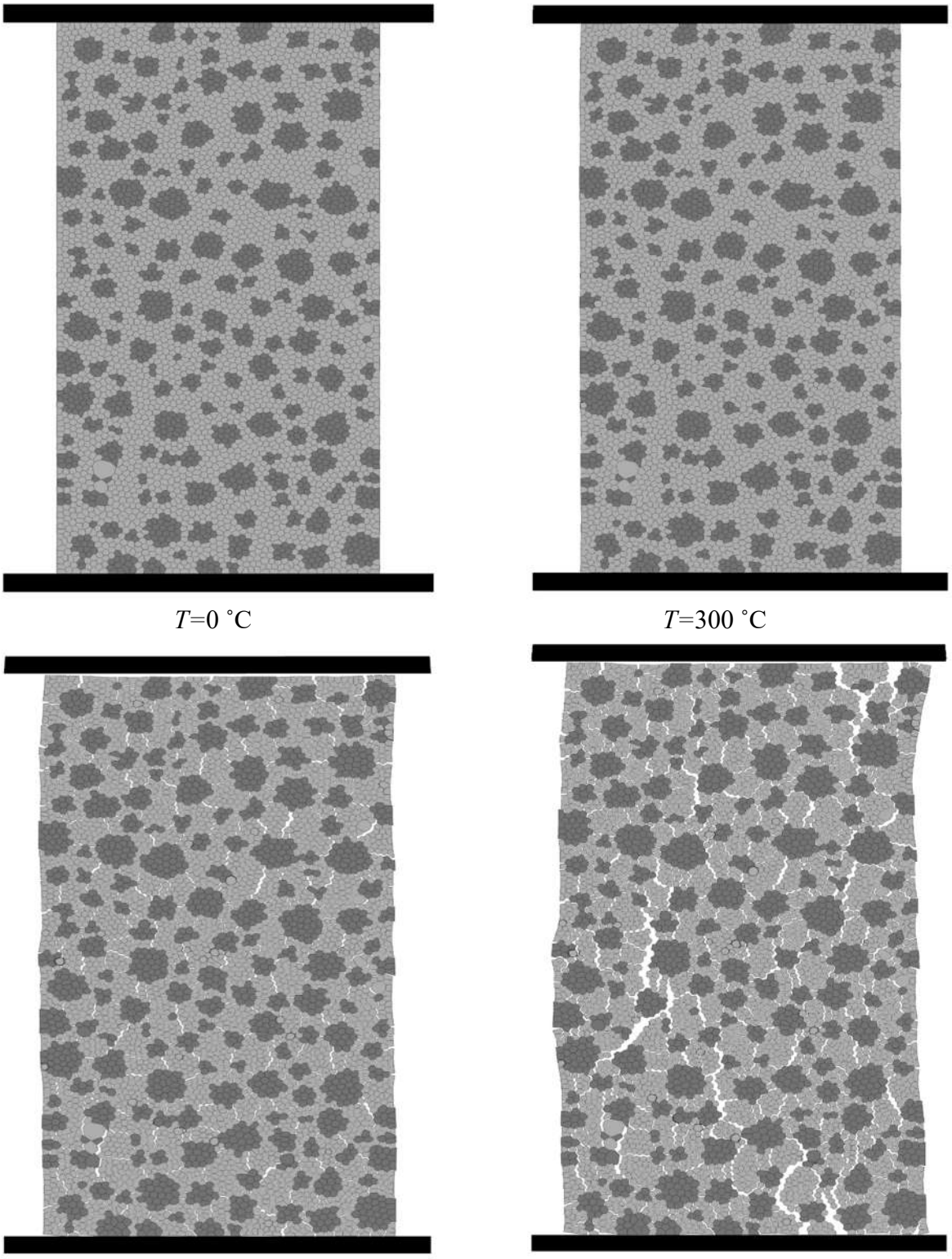

Figure 13. Fracture patterns in thermo-mechanical simulation ($\sigma/f_{c,25}$=0).

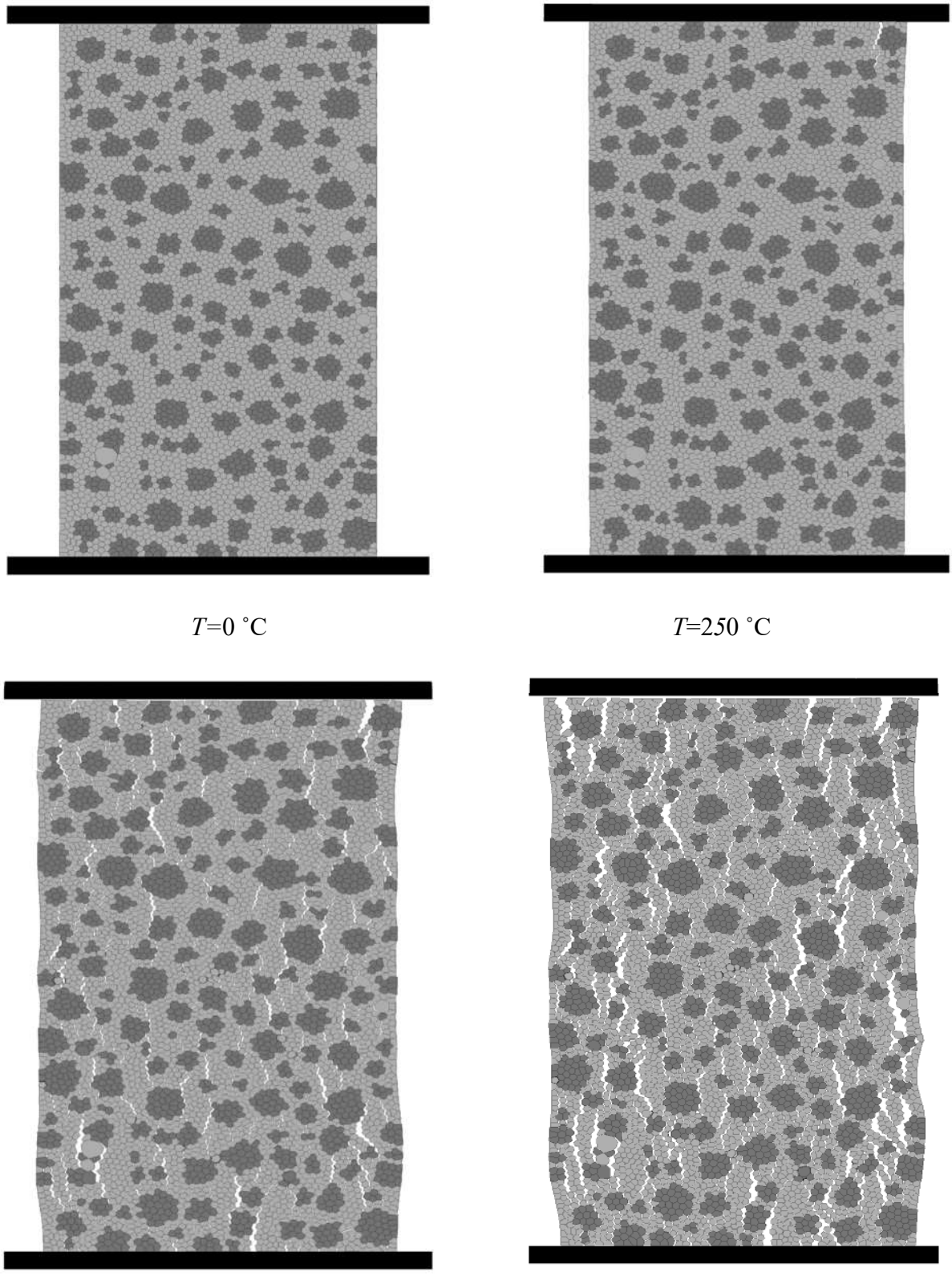

Figure 14. Fracture patterns in thermo-mechanical simulation ($\sigma/f_{c,25}$=0.225).

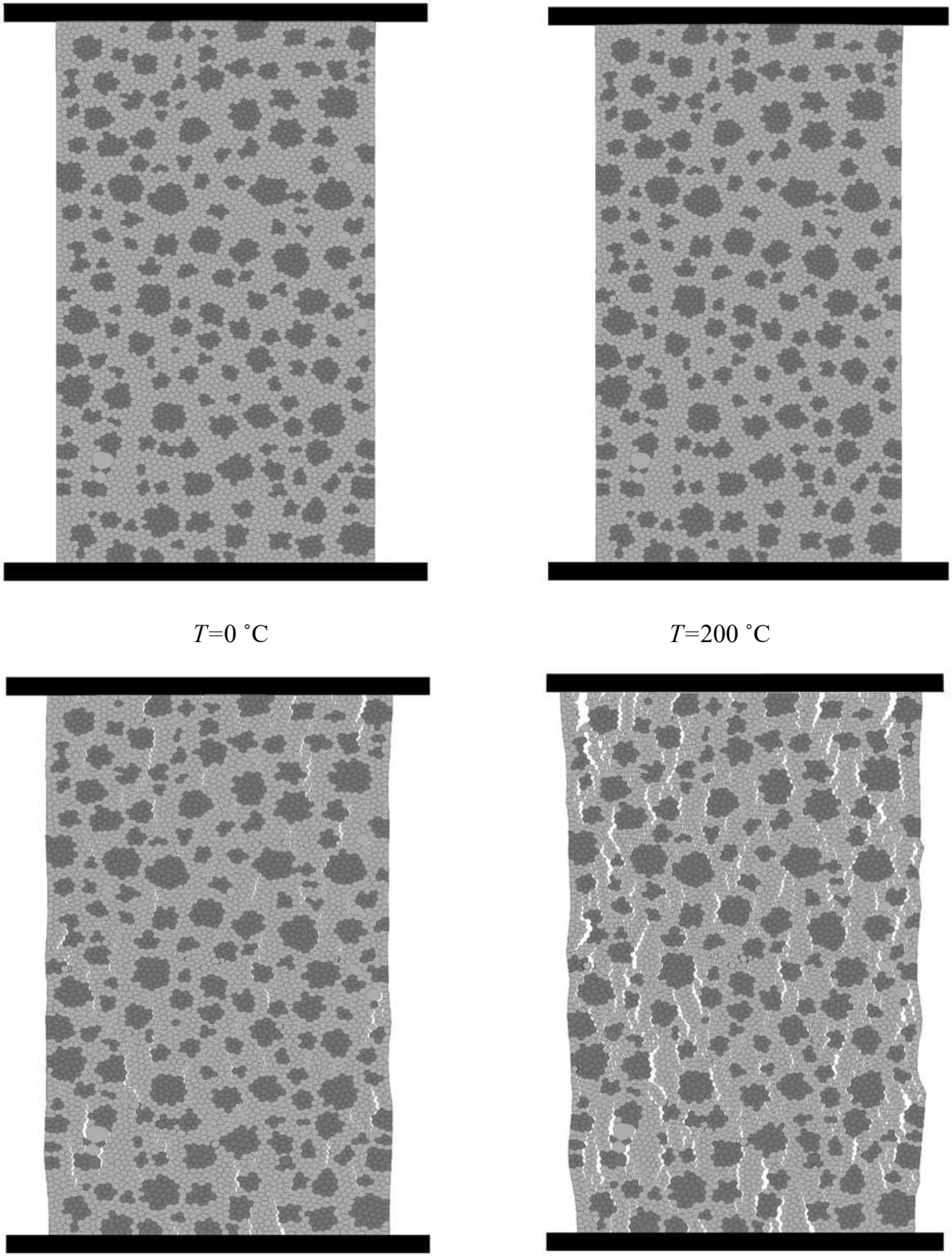

Figure 15. Fracture patterns in thermo-mechanical simulation ($\sigma/f_{c,25}$=0.445).

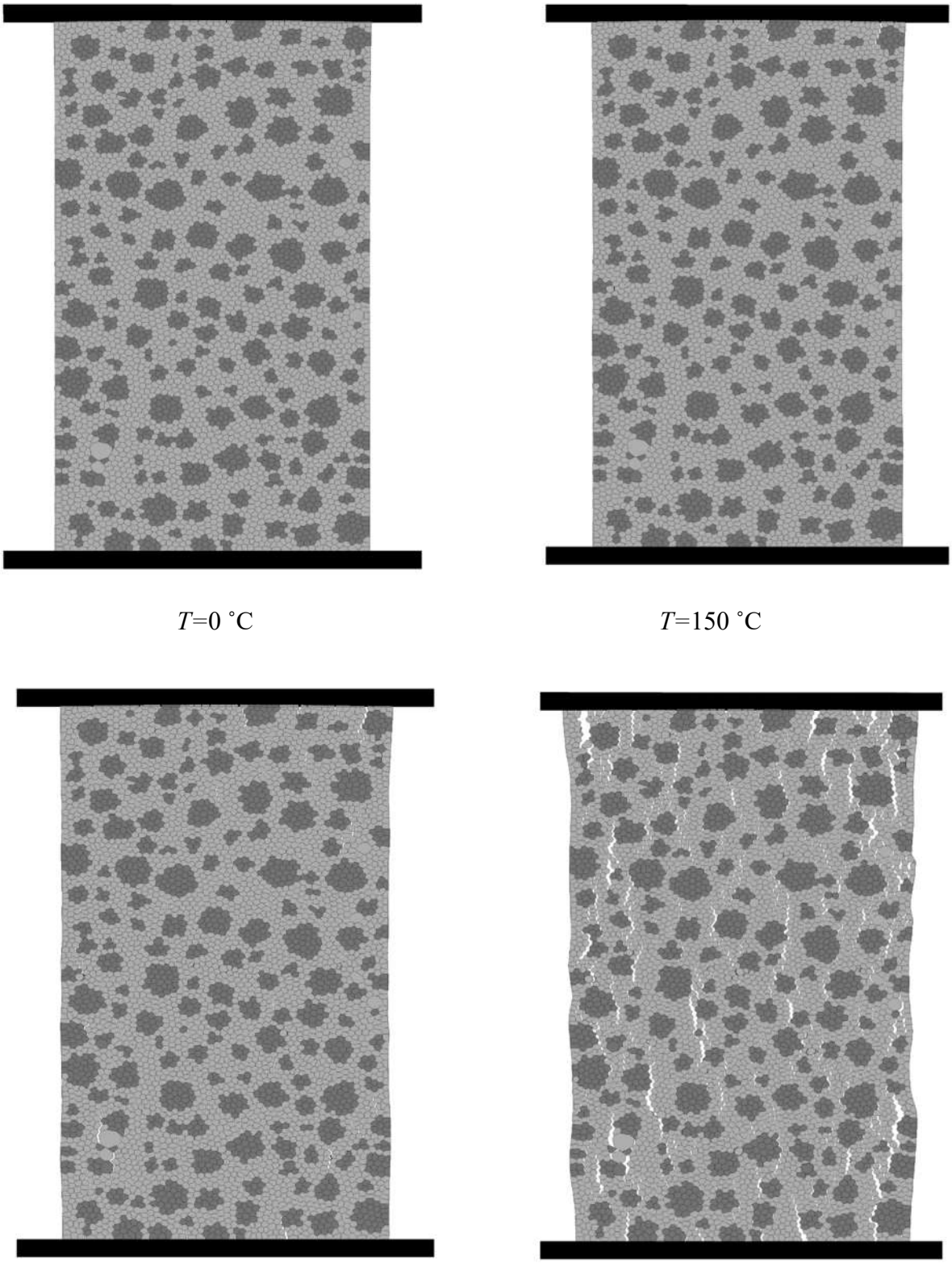

Figure 16. Fracture patterns in thermo-mechanical simulation ($\sigma/f_{c,25}$=0.675).